

pubs.acs.org/cm Article

Eu₅Al₃Sb₆: Al₄ Tetrahedra Embedded in a Rock-Salt-Like Structure

Published as part of the Virtual Special Issue "John Goodenough at 100".

Allan He, Zihao Shen, Haozhe Wang, Weiwei Xie, Zhen Wang, Luis Garay, James C. Fettinger, Raphaël P. Hermann, Yimei Zhu, Valentin Taufour, and Susan M. Kauzlarich*



Cite This: Chem. Mater. 2022, 34, 5009-5019



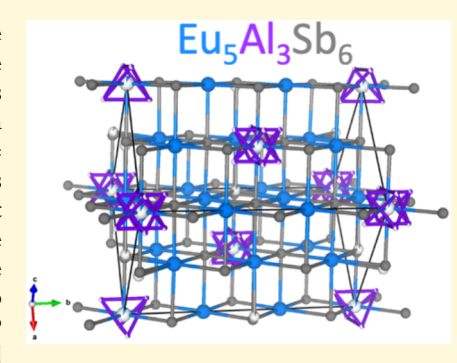
ACCESS |

III Metrics & More

Article Recommendations

s Supporting Information

ABSTRACT: The new Eu₅Al₃Sb₆ phase has been successfully synthesized as a pure phase through Sn flux methods yielding large, high-quality crystals. This structure type features disordered Al clusters that appear in the form of dual tetrahedra. It crystallizes in the monoclinic C2/m space group exhibiting a rock-salt-like Eu–Sb framework with [Al₄] tetrahedra replacing some of the cationic Eu atoms (space group: C2/m, a=8.151(1) Å, b=14.181(2) Å, c=8.145(1) Å, $\beta=109.577(2)^\circ$). The structure models the [Al₄] as dual tetrahedra with the Al atom sites 37.5% occupied along with Eu present on the central site at 8% occupancy and the remainder of the site being vacant. The presence of the [Al₄] cluster is further supported by HRTEM. Electronic structure calculations show that this material is a semimetal with observed band crossings close to the Fermi level. Strong Al–Sb antibonding interactions were found from COHP calculations close to the Fermi level and provide the rationale for the deficiency of the Al



cluster. Mössbauer spectroscopy on Eu-151 and Sb-121 provides oxidation states of 2+ and 3- along with the local environment. Magnetic susceptibility measurements can be described well with a Curie-Weiss law where an effective moment of 7.80 μ_B /mol Eu is obtained, consistent with Eu²⁺, and show canted antiferromagnetic behavior below 10 K. Temperature dependent resistivity shows a Kondo-like low-temperature upturn caused by enhanced scattering of the itinerant electrons with the 4*f* orbitals of Eu.

■ INTRODUCTION

Zintl phases have been shown to be a promising field for material discovery. These are charge balanced compounds where the combination of ionic and covalent bonding can lead to the formation of extremely complex structure types such as $Yb_{14}MnSb_{11}^{\ \ 1}$ and $Yb_{21}Mn_4Sb_{18}^{\ \ 2,3}$ and can exhibit a whole range of interesting physical phenomena. This includes high thermoelectric performance, intermediate valent behavior, Kondo type magnetism, superconductivity, topological behavior, and more. The variety in physical phenomena stems from the large number of possible structures that fall within the Zintl formalism. A new structure type and compound with the nominal stoichiometry of $Eu_5Al_3Sb_6$ has been discovered. The structure features disordered $[Al_4]$ clusters in an otherwise ordered rock-salt-type Eu-Sb framework where the Al clusters replace some of the Eu atoms.

These kinds of triel clusters are rarely seen in the solid state with only a few examples known in the literature such as the $Sr_{14}Al_8Ge_3$ phase and $Ni_{20}Al_3B_6$. Understanding the nature of triel clusters has been a subject of intense investigation in the organometallic community where work has been done on large Al clusters such as the iodized Al_{13} and Al_{14} clusters, as well as characterization of triel tetrahedra (including Al_4 tetrahedra). These clusters have exhibited unique behavior with electronic properties that are fundamentally different from bulk metals. For example, the Al_{13} cluster has been found to act as a

superhalogen whereas Al₁₄ can behave like an alkaline earth metal. Although these clusters have been shown to exist in the gas and solid phase, the additional complexity of clusters in a solid state structure impact bonding and can lead to a diversity of possible properties. 16

The idea of using defect chemistry for electrical property tuning has been used in the thermoelectric community for carrier concentration manipulation where, depending on the type of vacancy, the carrier concentration can be shifted higher or lower. Vacancies have been shown to control the electronic properties of oxides and clathrates and play an important role in property optimization. The inherent defects present in this structure type may make it ideal for property tuning. This new phase has the potential for realizing topological behavior through careful defect concentration tuning where band crossing is shown in the electronic structure calculations.

Herein, we report the synthesis, crystal structure, electronic structure calculations, magnetic susceptibility, electrical resistivity, and heat capacity studies for the Eu₅Al₃Sb₆ compound.

Received: January 29, 2022 Revised: May 10, 2022 Published: May 25, 2022





EXPERIMENTAL SECTION

Synthesis. Single crystal growth was completed using Sn flux. Large single crystals of this phase were grown where elemental Eu pieces (Ames Laboratory, 99.999%), Al shot (Alfa Aesar, Puratronic, 99.999%, 4–8 mm), Sb shot (Alfa Aesar, 99.999%, 6 mm), and Sn shot (Alfa Aesar, 99.99%, 1–3 mm) were loaded into Canfield Al_2O_3 crucibles with loading composition of $Eu_3Al_5Sb_3Sn_{15}$ with the original intent to prepare Eu_3AlSb_3 , a potential structural analogue of Yb_3AlSb_3 . ²¹ Quartz wool was placed on both the top and the bottom of the crucible, and the reaction was sealed into evacuated quartz tubes. The sample was heated to 1050 °C at 100 °C/h, allowed to dwell for 12 h, and then cooled slowly to 750 °C at 2 °C/h, after which the crucible was inverted and centrifuged to remove the molten tin to yield the crystals shown in Figure 1. No further purification of the sample was performed.

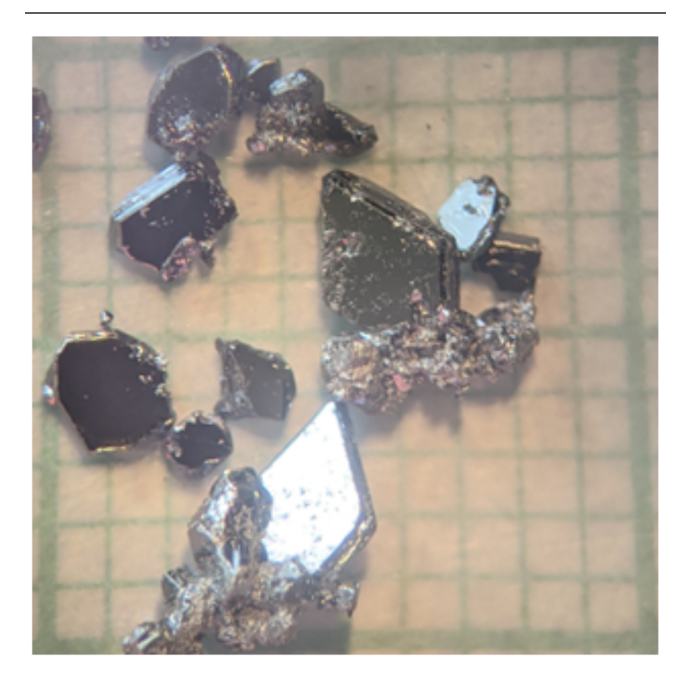


Figure 1. Representative single crystals obtained from flux experiments. One grid square is $1 \text{ mm} \times 1 \text{ mm}$.

Considering Sb as the limiting reagent with 0.6677 g, the theoretical yield is 1.4472 g of product. The experimental mass of the product is 1.2074 g, giving rise to a percent yield of 83.72%. This reaction procedure was reproduced several times, and since the yield of crystals was high and powder diffraction showed that it was phase pure, the flux synthesis was presumed to be optimized.

Single Crystal X-ray Diffraction. Single crystal diffraction data were collected at 100 K using a Bruker Apex Duo diffractometer with Mo K α (λ = 0.71073 Å) radiation. Crystals were selected under Paratone oil, mounted on a MiTeGen MicroLoop, and then placed in the cold nitrogen stream at 90 K. Crystals are mildly air-sensitive and tarnish over time. The crystals had plate morphology and were highly black and reflective (see Figure 1). Absorption corrections were applied using SADABS. Space group determination was done using XPREP, and structural solutions were completed through direct methods with SHELXT and refined using the SHELXL software. Initial structural solutions assumed a Cm space group that yielded a Flack parameter closer to 0.5, which suggested twinning and/or a centrosymmetric space group. A structure determination was then obtained in the centrosymmetric space group C2/m using SHELXT and a variety of site occupancy tests. All aluminum atoms were allowed to freely refine and converge close to the ideal 37.5% occupancy and were then restricted as such. The partially occupied Eu1 site was allowed to freely refine. Data collection parameters and atomic coordinates are provided in Supporting Information, Tables S1 and S2.

Data sets for several different crystals were collected to look for a superstructure and investigate the possibility of a modulated structure component. We tested the possibility of an Al rather than an Eu atom on the Eu1 site. When placing Al on the site and freely refining the occupancy, the *R*-values increase significantly along with the weighting scheme indicating a poor model. We investigated the possibility of a mixed occupancy Eu/Al Eu1 site, and the Al % goes to zero with the Eu occupancy converging at 8%. The structural model described herein provides an average structure with the lowest *R* values. Zone images overlaid with the calculated diffraction peaks for the monoclinic C2/m structure are provided in the SI, Figures S1–S3.

Transmission Electron Microscopy. Samples for TEM analysis were crushed in an agate mortar and deposited directly onto holey carbon copper grids. The scanning transmission electron microscopy (STEM) imaging and electron diffraction were performed on a 200 kV JEOL ARM electron microscope at Brookhaven National Library equipped with double aberration correctors and a cold field emission source. The high-angle annular dark-field (HAADF) STEM images were collected with a 21 mrad convergent angle (30 μ m condenser aperture) and a collection angle of 67–275 mrad.

Powder X-ray Diffraction. Powder X-ray Diffraction (PXRD) data were collected on a Bruker D8 Advance Eco Diffractometer using Cu $K\alpha$ radiation from $2\theta = 20-80^{\circ}$ at room temperature in air. The crystals were ground in air and plated on a zero-background holder. Rietveld refinements were completed using the TOPASS software.

Compositional Analysis. Single crystal samples were placed flat on carbon tape for elemental analysis. Energy dispersive X-ray spectroscopy data was collected with a FEI Scios DualBeam SEM/FIB with a window-less Oxford Instruments X-max50, 50 mm² silicon drift detector. Secondary electron images were collected using a 20 kV and 1.6 nA electron beam.

Electronic Structure Calculations. The hypothetical "Eu₅Al₄Sb₆" with a fully occupied tetrahedral Al₄ cluster instead of partially occupied Al₄ cluster was employed to perform the electronic structure calculations. Experimental structural parameters were employed. Tight-Binding, Linear-Muffin-Tin Orbital Atomic Spheres Approximation (TB-LMTO-ASA) was used to generate the density of states (DOS) and orbital Hamiltonian population (COHP) curves, in which electrons on Eu 4f orbitals were treated as core electrons. ^{22,23} To obtain more accurate electronic structure information, the Wien2k program, which implements the full-potential linearized augmented plane wave (FP-LAPW) method, was used to generate the band structure. On-site U = 6 eV was used for Eu f-orbitals. ²⁴ The spin—orbit coupling (SOC) was included on Eu and Sb atoms self-consistently in the calculations of electronic structures with a Monkhorst—Pack k-point mesh $8 \times 4 \times 8$ with the cutoff energy 500 eV.

Mössbauer Spectroscopy. Europium-151 and antimony-121 Mössbauer spectra were measured at room temperature using a constant acceleration Mössbauer drive (Wissel GmbH), with the velocity in the -20 to +20 mm/s range, calibrated using a cobalt-57 source and alpha-iron foil; the sources, 151 SmF $_3$ and Ca 121 SnO $_3$, respectively, were kept at room temperature. A NaI:Tl scintillator was used as the detector for antimony-121; 37.2 keV and the escape peak were selected, and Sb Kα radiation was excluded in the pulse height analysis. The sample was prepared by mixing 75 mg/cm 2 of powder with boron nitride. Data and isomer shifts are reported relative to the respective source.

Magnetic Susceptibility. Magnetization measurements were performed in a Quantum Design Magnetic Properties Measurement System (MPMS) from 2 to 300 K and up to 7 T. The crystals chosen for magnetic measurements had their unit cells confirmed through single crystal XRD prior to measurement. The crystals were aligned with the *c*-axis parallel to the applied field.

Electronic Transport and Magnetoresistance. DC resistivity and magnetoresistance were measured in a Quantum Design Physical Property Measurement System (PPMS) from 0 to 0.5 T using the fourlead method from 2 to 300 K. Contacts were made with the platinum wire held in place by silver epoxy (see SI, Figure S4). The electrical resistivity was measured in the *ab*-plane. There was no evidence for residual Sn in the low temperature measurements.

Heat Capacity. Heat capacity measurements were done in a Quantum Design PPMS from 2 K - 300 K. Low temperature heat capacity from 0.6–20 K was measured with a QD PPMS with He-3 refrigerator system. There was no evidence for residual Sn in the low temperature measurements.

RESULTS AND DISCUSSION

Crystal Structure. $Eu_{5.08}Al_3Sb_6$ (referred to hereafter as $Eu_5Al_3Sb_6$) crystallizes in the monoclinic C2/m space group, and the structure features a rock-salt-like Eu-Sb framework with two interpenetrating partially occupied $[Al_4]$ tetrahedra replacing some of the cationic Eu atoms (Figure 2). The $[Al_4]$ tetrahedra

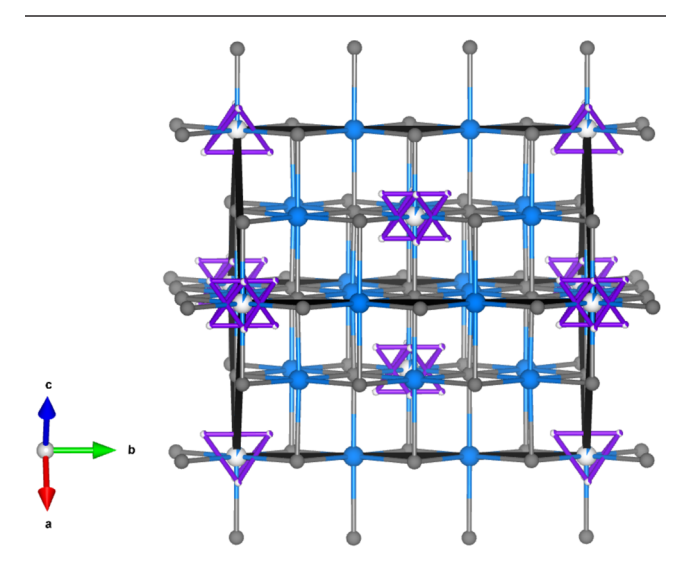


Figure 2. Unit cell of the Eu_{5.08}Al₃Sb₆ structure where Eu atoms are in blue, Sb atoms are in gray, and Al atoms are in purple (space group: C2/m, a = 8.151(1) Å, b = 14.181(2) Å, c = 8.145(1) Å, $\beta = 109.58(1)^\circ$) shown without Sb2 disorder for clarity (for views with Sb2 disorder shown, refer to SI, Figures S5 and S6). The occupancy of the site (Al/Eu) is indicated by the shading of the sphere (37.5/8%).

have an average bond length of around ${\sim}2.65$ Å, slightly shorter than other [Al₄] containing compounds reported in the literature 9,15 but consistent with distances found in Al₄ clusters in ternary intermetallics 25 and a polyhedral volume of ${\sim}2.185$ ų. The Al–Sb bond distances are 2.652–2.730 Å, shorter than those found in the tetrahedrally coordinated Al of AlSb (2.83 Å). 26

A close-up of the Al moiety is provided in Figure 3a, where all Al (Al1, Al2, Al3) atoms are partially occupied 37.5% of the time, and the central Eu1 atom was refined to be present 8% of the time. The disorder can be rationalized as having an [Al₄] cluster on the site in either one or the other orientation 75% of the time with a Eu atom present 8% of the time (not concurrent with the [Al₄] cluster) and a vacancy for the remainder. The residual electron density was found to be close to the Sb2 site and was modeled as site disorder with another Sb site, Sb2B. The Sb2/ Sb2B site was refined to be occupied 92%/8% of the time. This site disorder is likely due to the occasional presence of Eu (8%) in the Eu1 site. For a closeup view of the Sb2 disorder, refer to the SI, Figure S5, and for a unit cell view, refer to the SI, Figure S6. The Eu1 and Al atoms cannot exist simultaneously as the bond distance is too small (~1.6 Å). Select bond distances are provided in Table 1 below.

The presence of the partially occupied Eu atom changes the nominal stoichiometry of Eu₅Al₃Sb₆ to Eu_{5,08}Al₃Sb₆. In Figure

3b, the two interpenetrating $[Al_4]$ tetrahedra are colored purple and pink for clarity.

In Figure 3c, a close-up of one orientation of the tetrahedra is shown with select Al-Al distances. Note that the vertices of the two tetrahedra in conjunction form a cube; however, the Al-Al distances of adjacent Al atoms in the cube are too small (\sim 1.85 Å) for all Al atoms to be present at the same time. Therefore, the presented structural model is such that the tetrahedra exist only in one orientation at a time, and only when the central Eu atom is not present. Since the tetrahedra reside within a Sb₆ octahedron, there are no structural restrictions for one orientation of the $[Al_4]$ over the other. Therefore, the best model provides a dual tetrahedra in the center. Figure 3d shows the coordination environment of the Eu1/[Al4] dual tetrahedra in a polyhedral view emphasizing that the Al tetrahedra are positioned within the Sb octahedra such that each vertex of the Al tetrahedra point toward the center of a unique octahedral face. This is the most sensible configuration to minimize Coulombic repulsion within the structure and provides stabilization. The coordination environment of Eu1 with select bond distances is shown in Figure 3e, where we note that the Al atom does not sit precisely in the center of the octahedral face but is slightly below the plane of the octahedral face. The rare earth transition metal aluminides of the stoichiometry $RE_4Pd_9Al_{24}$ (RE = rare earth) contain a disordered rare earth/Al layer, in which Al₃ triangles mix on the rare earth sites.²⁷ The Al₃ triangles and rare earth sites are each partially occupied somewhat reminiscent of the Al₄ tetrahedra and Eu²⁺ in this Eu₅Al₃Sb₆ compound. The Eu-Sb bond distances presented are very similar to other binary Eu–Sb phases such as Eu₅Sb₃, ²⁸ Eu₁₁Sb₁₀, ²⁸ and Eu₂Sb₃. ²⁸ The rocksalt-like nature of this compound is reminiscent of that of YbSb,²⁹ a rare-earth antimonide compound that features the NaCl structure type as well. All the other atomic site (Eu2, Eu3, Eu4, Al cluster, Sb1, Sb2) coordinations are presented in the SI, Figures S7-S9.

DFT calculations have been performed on free aluminum clusters that have found that the ground state structural isomer of an Al₄ cluster is a planar rhombus in a triplet electronic spin state while the Al₄ tetrahedral clusters are the least energetically favorable form. $^{30-32}$ The ab initio calculations predict a bond length of 2.74 Å for the tetrahedral cluster (multiplicity of 5)³¹ or a bond length of 2.692 Å in a triplet state. 32 The bond length found experimentally for the Al tetrahedron is around 2.65 Å, slightly smaller than either of the calculations but may be a requirement of the Sb octahedron in which it is centered. In the case of an Al₄H₂ or Al₄H₄ cluster, when hydrogen is attached to the tetrahedral Al atom vertices, the bond lengths of the Al cluster decrease so that the Al-Al distances are 2.66 Å and 2.60 Å, respectively, and the overall stability of the cluster increased.31 Since the Al-Al bond length observed in the Eu₅Al₃Sb₆ compound (2.65 Å) is less than that observed for the calculated, free Al₄ tetrahedra in any spin configuration and because the [Al₄] cluster is not observed in the ground state structure (planar rhombus), there must be a source of stabilization. It is presumed that like the hydrogenation case each face of the Sb octahedral cage could provide charge stabilization to the [Al₄] cluster, allowing it to adopt the observed tetrahedral geometry, and therefore the cluster results in the shorter than expected bond distance. As mentioned previously, it is expected that the Al tetrahedra can only exist in high energy states.

Given that other Eu–Al–Sb phases such as $\mathrm{Eu_5Al_2Sb_6}^{33}$ and $\mathrm{Eu_{14}AlSb_{11}}^{34}$ and similar compounds are all Zintl phases, it may

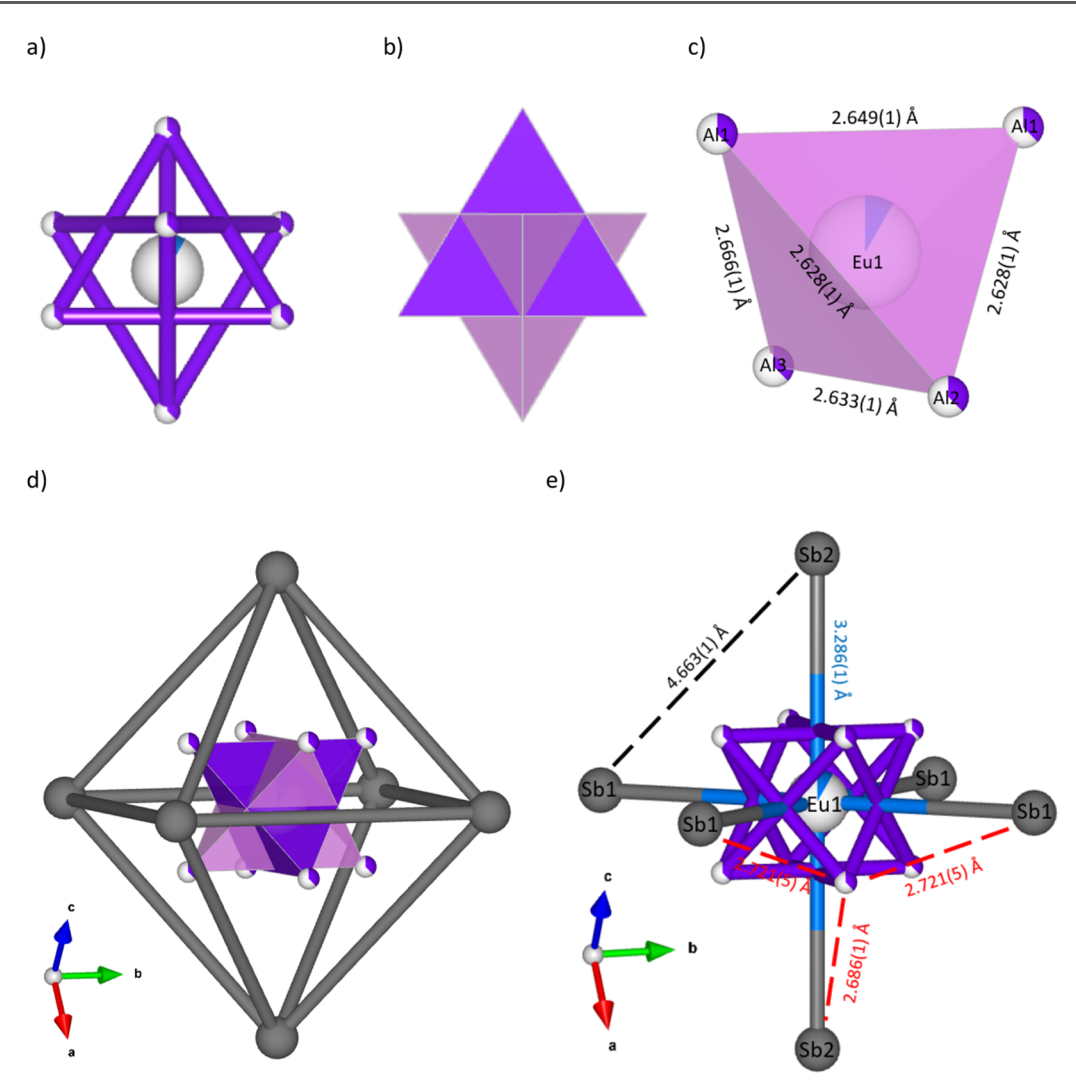


Figure 3. Close-up view of the (a) two interpenetrating [Al₄] tetrahedra and the central site deficient Eu atom (Eu1), (b) dual tetrahedra color schemed for clarity, (c) single tetrahedron, (d) Eu1 coordination showing arrangement of the dual tetrahedra inside the Sb octahedral cage, and (e) Eu1 coordination site environment. Shown without Sb2 disorder; refer to SI, Figures S7–S9, for more details.

Table 1. Selected Bond Distances for Eu₅Al₃Sb₆

Eu atom pairs		distance (Å)	Al atom pairs		distance (Å)	Sb atom pairs		distance (Å)
Eu2-	$Sb1 \times 2$	3.3350(5)	Al1-	Al2	2.628(9)	Sb1-	Al1	2.684(6)
	$Sb1 \times 2$	3.3457(6)		Al1	2.65(1)		Al1	2.713(6)
	$Sb2 \times 2$	3.3250(8)		Al3	2.666(9)		Al2	2.720(5)
	$Al2 \times 2$	3.501(7)		Sb1	2.684(6)		Al3	2.730(4)
	$Al1 \times 2$	3.534(6)		Sb1	2.713(6)		Eu1	3.3009(5)
Eu3-	$Sb2B \times 2$	3.12(1)	Al2-	Al1	2.628(9)	Sb2-	Al3	2.652(8)
	$Sb1 \times 4$	3.3294(5)		Al3	2.63(1)		Al2	2.686(9)
	$Sb2 \times 2$	3.371(1)		Sb2	2.686(9)		$Al1 \times 2$	2.720(6)
	$Al2 \times 2$	3.509(9)		Sb1	2.720(4)		Eu2	3.3250(8)
	$Al3 \times 2$	3.523(9)					Eu2	3.3251(8)
Eu4-	$Sb2B \times 2$	3.155(9)				Sb2B-	Eu3	3.12(1)
	$Sb1 \times 2$	3.3231(5)					$Eu4 \times 2$	3.155(9)
	$Sb1 \times 2$	3.3336(6)					$Eu2 \times 2$	3.563(9)
	$Sb2 \times 2$	3.3604(8)						
	$Al3 \times 2$	3.515(6)						
	$Al1 \times 2$	3.529(5)						

be reasonable to approach the structure using Zintl electron counting and assume a charge balanced phase. In the unit cell, there are a total of 16 Al atoms (Al1 site: 8j, Al2 site: 4i, Al3 site:

4i), each at 0.375 occupation. Since Z = 2 for this structure, per formula unit, there are 8 aluminum atoms (two tetrahedra), where $8 \times 0.375 = 3$, the molar ratio of aluminum in the formula

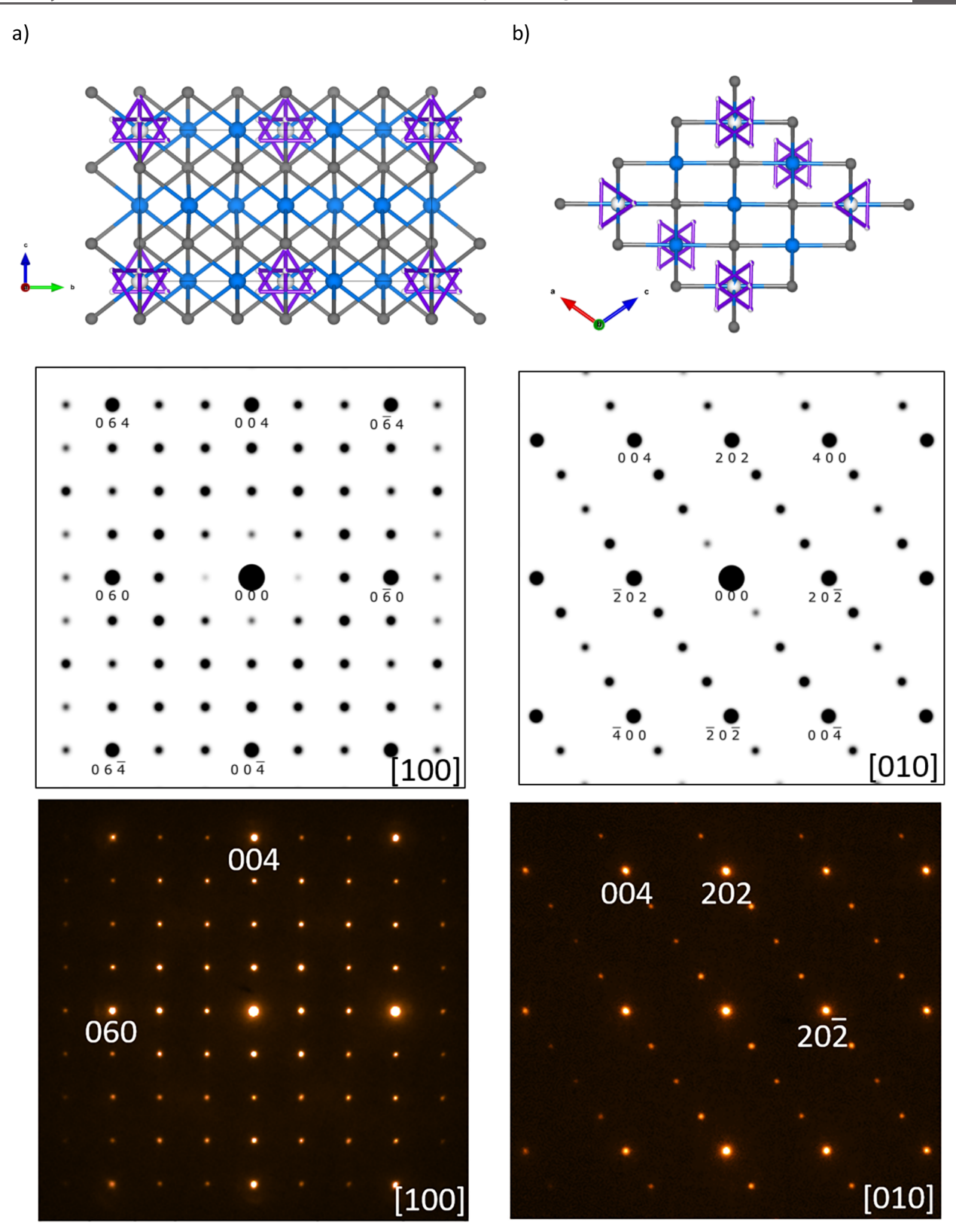


Figure 4. Projected crystal structures and electron diffraction patterns along the [100] direction ((a) column) and the [010] direction ((b) column). Top row: Projected crystal structures in real space. Middle row: Simulated electron diffraction patterns. Bottom row: Experimental selected area electron diffraction patterns.

unit. Assuming that the oxidation states of the Sb atoms are 3— and that the Eu atoms are 2+, then in the nominal $Eu_5Al_3Sb_6$ compound, an excess of 8 electrons must be accounted for by the two tetrahedron, meaning that each $[Al_4]$ tetrahedron must be

4+. In summary, the compound can be written as $(Eu^{2+})_5([0.375Al_4]^{4+})_2(Sb^{3-})_6$, where 0.375 arises from the site occupancy of 37.5%. However, it is also possible to think of this compound simply as the Al atoms being 3+ each with one of

the 3s electrons being itinerant in the material. The interaction of this itinerant electron with the local 4f states of Eu would result in heightened carrier scattering that is apparent only at low T, where quantum phenomena dominate. This corresponds well to the observed increase in resistivity at low T. Under the itinerant electron framework, the $[Al_4]$ cluster would have S=0 and a multiplicity of 1 (singlet) with all electrons paired, necessitating the existence of a stabilization source (i.e., the Sb octahedra) in order for this structure to be realized since it has been shown that the singlet spin configuration of the Al tetrahedra is the least energetically stable isomer. 32

In either structural framework, there would be a deviation from the Zintl precise structure as there exists a partially occupied Eu site (Eu1) when the [Al₄] clusters are not present. This would result in more electrons being donated into the structure to make it more n-type, which is what we observe in Hall carrier concentration measurements (see below).

Transmission Electron Microscopy. Selected area electron diffraction (Figure 4) and HAADF-STEM imaging (Figure 5) were performed to further confirm the structure obtained

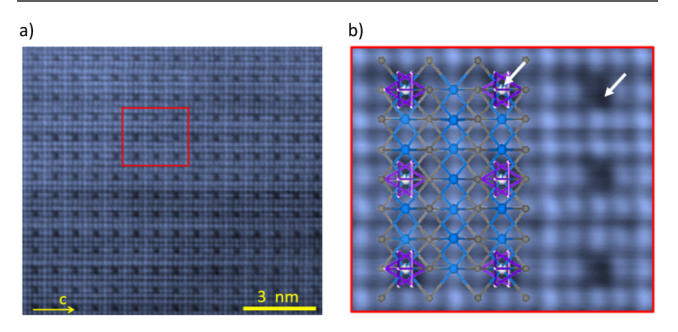


Figure 5. (a) False-colored HAADF-STEM image of $\operatorname{Eu}_5 \operatorname{Al}_3 \operatorname{Sb}_6$ single crystals taken along the [100] direction. (b) Enlarged image from the boxed area in (a). The crystal model is superimposed on the experimental image showing the same structure. The white arrows highlight the dark contrast (low Z), indicating the locations of the [Al₄] clusters denoted by purple bonds and the Eu (8% occupancy, center).

from X-ray crystallography. The simulated and experimental electron diffraction data show good agreement and further support the single crystal structural model. In the Z-contrast HAADF image shown in Figure 5, the Eu (Z=63) layers are brighter than the Sb ones, which agrees well with the superimposed unit cell. Since Al (Z=13) is much lighter than Eu and Sb, the Al clusters are directly visible in the Z-contrast image as a dark contrast, and since Eu is only present as 8% of the site with the remainder being vacancies, there is no evidence for the presence of Eu in the image.

Powder X-ray Diffraction. Entire batches of crystals isolated from the Sn flux experiments were ground up and analyzed through powder X-ray diffraction (PXRD). Rietveld refinement of the PXRD data (Figure 6) show that the single crystal synthetic scheme presented here yields samples that are pure phase. The obtained lattice parameters from the refinement (a=8.1642(4) Å, b=14.2129(5) Å, c=8.1716(4) Å, $\beta=109.61(1)^\circ$) are slightly larger than those obtained from the single crystal refinement due to the difference in data collection temperatures. In the single crystal analysis, the presence of weak reflections seems to indicate that the unit cell could be multiple times larger or modulated. It should be noted that, despite this, the current average structural model has an R_1 value of 0.0320 and is sufficient for the current study.

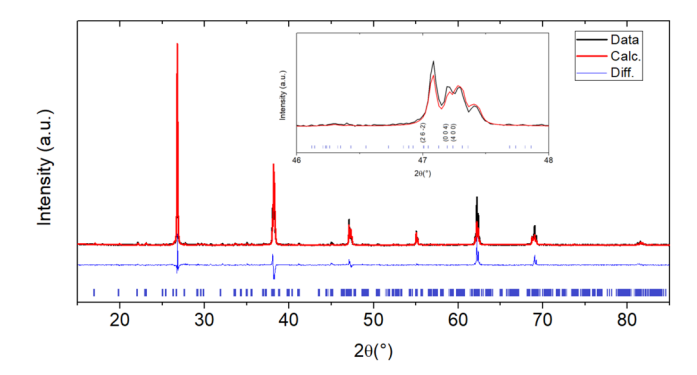


Figure 6. Powder X-ray diffraction pattern for Eu₅Al₃Sb₆ single crystals grown from Sn flux ground into powder showing Rietveld refinement with the obtained single crystal structure (Crystallographic information file, SI) file. The inset shows an enlarged version of the refinement with the $(26\overline{2})$, (004), and (400) reflections indicated. The data are presented in black, calculated spectrum in red, and difference in blue.

Compositional Analysis. Single crystals were analyzed using SEM-EDS (Figure 7). Compositions of the crystals were experimentally found to be 34.8(2)% Eu, 22.9(4)% Al, and 42.3(3)% Sb, which are within error of the nominal composition for this phase (nominally 36.0% Eu, 21.3% Al, 42.6% Sb). The EDS spectrum can be found in the SI, Figure S10).

Electronic Structure Calculations. To further understand the structural stability, Al cluster occupancies, and electronic properties of Eu_{5.08}Al₃Sb₆, we performed first-principles calculations based on the structure of a hypothetical model "Eu₅Al₄Sb₆" with a fully occupied Al₄ tetrahedral cluster to investigate the electronic density of states (DOS) and crystal orbital Hamilton population (COHP) curves which were calculated by using the tight-binding linear-muffin-tin orbital approximation. Figure 8a illustrates the total and partial DOS with an emphasis on Al-Al and Al-Sb interactions. The DOS ranging from -4.0 to +4.0 eV mainly consist of s and p orbitals contributed from Al, Sb, and Eu. The Fermi level for Eu_{5,08}Al₃Sb₆ is around 1.2 eV below in "Eu₅Al₄Sb₆", where the nearly zero DOS was observed in Figure 8a. That is consistent with the experimental transport properties of the crystals (see discussion below). According to the corresponding COHP curves in Figure 8b, the wave functions contributing to the Fermi level of " $Eu_5Al_4Sb_6$ " have strong Sb-Al antibonding character. The band gap at \sim 1.2 eV below the Fermi level is associated with optimization of Sb-Al orbital interactions in the system. Moreover, such strong Sb-Al antibonding may also cause the large Al deficiency on the cluster to reduce the Sb-Al interactions in Figure 8d. In addition to the chemistry bonding interaction, the Eu-based semimetals are well-known for hosting magnetic topological properties. The full band structure was calculated based on the generalized gradient approximation (GGA) and GGA with SOC (GGA+SOC) methods to better understand the electronic structure, shown in Figure 8c. The bands between -2 and +1 eV (0 eV = Fermi level for 52 valence electrons) are primarily contributed from the hybridization of Sb 5s and 5p bands and Al 3s and 3p bands. Below -2 eV are \sim 2 eV wide bands comprising mainly Eu 4f orbital contributions that are on-site U dependent. A noticeable bandgap was observed at approximately −1.2 eV (~49 valence electrons) below 0 eV, which is only \sim 0.03 eV wide. According to the band analysis, the wave functions contributing to this area (Fermi level to 1 eV below Fermi level) are mainly from Sb atoms. When SOC effects

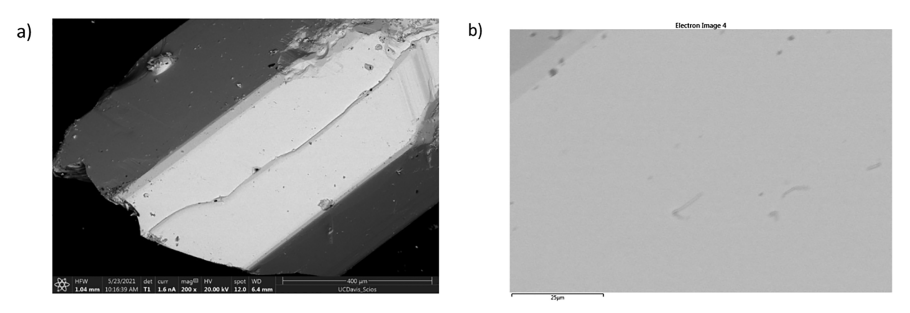


Figure 7. Secondary electron image collected with a 20 kV electron beam on the single crystals showing (a) an overall view of the crystal and (b) an enlarged view of the surface.

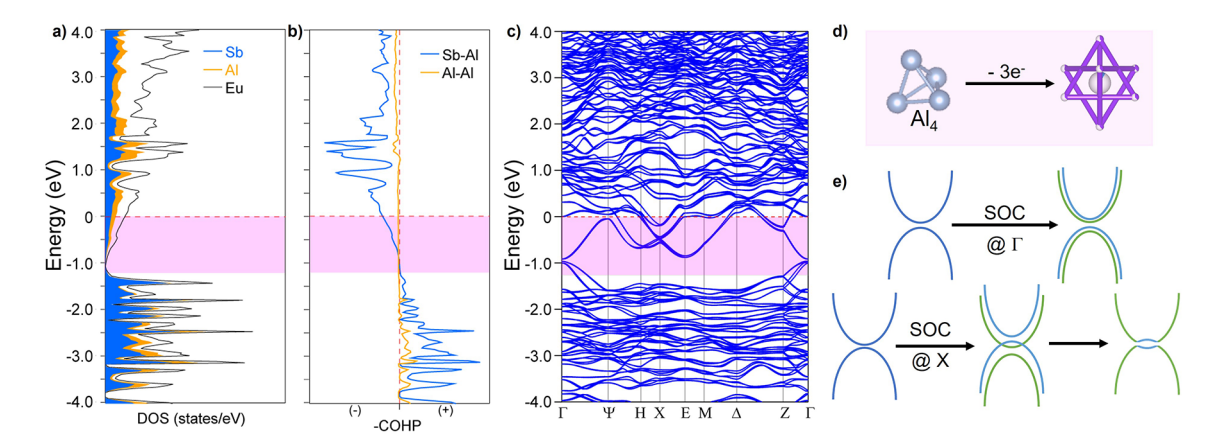


Figure 8. Electronic structure of hypothetical "Eu₅Al₄Sb₆". (a) Density of states (DOS) from the LMTO method. (b) COHP curves and (c) band structure with spin—orbit coupling (SOC) effects on Eu and Sb atoms, spin polarization (AFM), and on-site U = 6 eV on Eu 4f. The red dashed line is the Fermi level (0 eV) for 52 valence electrons. The shaded pink area from -1.2 to 0 eV covers from 49 e⁻ to 52 e⁻ where the 49 e⁻ compound would correspond to being a semimetal. (d) Schematic for the structure–valence relationship in the shaded pink area in (a). (e) Illustration of spin—orbit coupling (SOC) effects on the band structure at the Γ (\sim 1 eV below E_F) and X (\sim 0.5 eV below E_F) points.

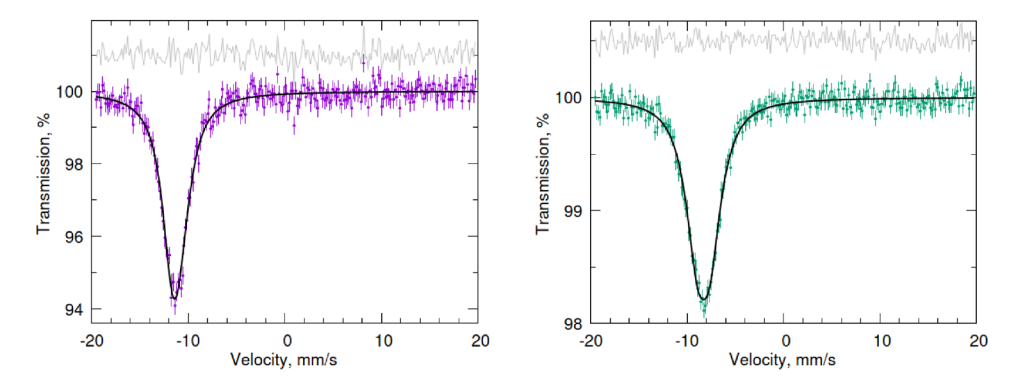


Figure 9. Europium-151 (left) and antimony-121 (right) Mössbauer spectra of Eu₅Al₃Sb₆ obtained at room temperature. Data with error bars are shown as points, fits as black lines, and differences as offset gray lines.

of Eu and Sb atoms are turned on, Eu-4f and Sb-s, p bands are split due to the Rashba effects. Moreover, when electronic interactions via LDA plus correlation parameter U (LDA+U) were considered in the calculations, the Eu-4f bands (split into the j=7/2 states and j=5/2 states by SOC) are shifted to 2.0–4.0 eV below $E_{\rm F}$. In addition, the strong SOC effect increases the gap associated with the band crossing points which arise from Sb-5s, p and Al-3s, p orbitals around the X point \sim 0.5 eV below the Fermi level. The strong SOC effect further enhances the band splitting of crossing states and flattening at the H, X, E, and M points near $E_{\rm F}$. Targeting this energy space where the band crossings occur through defect control or aliovalent substitution on the disordered Eu/[Al₄] sites could induce topological

behavior within this compound as illustrated in Figure 8e. Consistant with DOS and COHP curves calculated using LMTO-ASA, the Fermi level generated by the WIEN2k program for the Eu_{5.08}Al₃Sb₆ (~49 valence electrons) compound would be located exactly at the bandgap around -1 eV, which would make it a semimetal. However, the presence of the Eu atoms increases the valence electron count and would shift the Fermi level into the conduction band. This theoretical prediction is consistent with the experimental observations from resistivity measurements and the Hall carrier concentration (described in the following text).

Mössbauer Spectroscopy. The Eu-151 and Sb-121 Mössbauer spectra (Figure 9) show that all Eu ions have a 2+

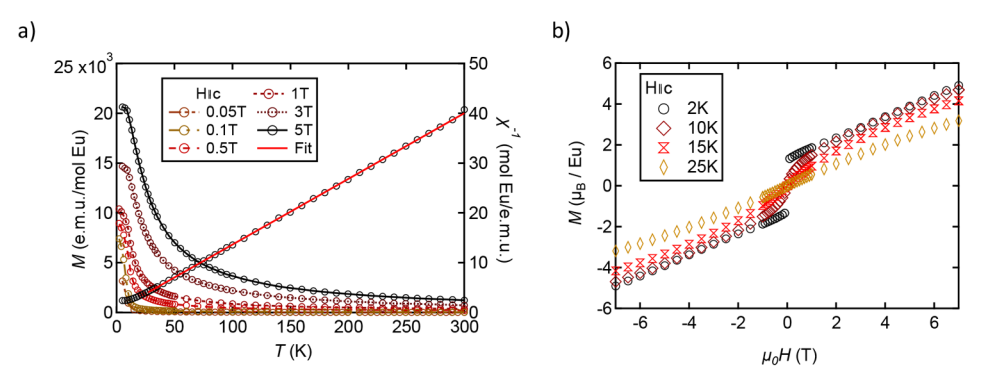


Figure 10. (a) Magnetization measurements as a function of field temperature at various applied magnetic fields parallel to the *c*-axis (H = 0.05 T, 0.1 T, 0.5 T, 1 T, 3 T, 5 T). The right axis shows the Curie–Weiss fit to the inverse susceptibility yielding a moment of 7.80 μ_B /Eu for the 5 T data. (b) Magnetization as a function of field up to 7 T.

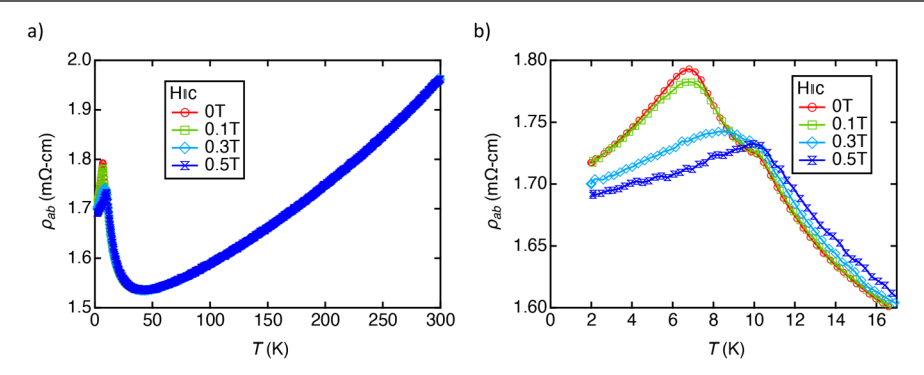


Figure 11. (a) In-plane electrical resistivity as a function of temperature at various applied fields parallel to the c-axis for the Eu₅Al₃Sb₆ single crystal. (b) Close-up of the region between 2 and 15 K that shows the AFM transition shifting to higher temperatures.

oxidation state (isomer shift $\delta = -11.31(2)$ mm/s, similar to Eu in Eu₁₄AlSb₁₁³⁴) and all Sb ions have a 3- oxidation state (δ = -8.30(2) mm/s, similar to Sb in AlSb³⁶) as suspected from the Zintl formalism. A fit of both spectra with a single Eu or Sb site reveals that the line shape is not a simple Lorentzian. For Eu, a small quadrupole splitting ($\Delta E_Q = -2.2$ (3) mm/s) suffices to obtain a good fit; for Sb using an asymmetry parameter, η is required ($\Delta E_{\rm O} = -3.7$ (3) mm/s; $\eta = 1$). The obtained fit parameters are certainly not unique and correspond to an average over the different sites. Because both fits account for the residuals ($\chi^2_{red} = 1$), it is unwarranted to use additional sites. Because the line width $(\Gamma_{Eu} = 2.6(1) \text{ mm/s}; \Gamma_{Sb} = 2.6(1) \text{ mm/s})$ is rather narrow, we can infer that there is little variation in the local coordination environment for Eu and Sb. This makes sense when comparing to the structure, where the Eu and Sb atoms adopt a rock-salt-like framework.

Magnetic Susceptibility. The magnetic susceptibility measurements are shown in Figure 10a. Magnetic susceptibility at 5 T was fit with a Curie—Weiss law, $\chi(T) = \frac{C}{T-\theta}$, to yield C = 7.604 and $\theta = -5.95$ K. The Curie constant (C) leads to an effective magnetic moment of $\mu_{\rm eff} = 7.80~\mu_{\rm B}$ /Eu. Given that the theoretical moment of Eu²⁺ is $7.94~\mu_{\rm B}$, there is good agreement with the obtained effective magnetic moment. At low magnetic field, the high temperature susceptibility (above $T_{\rm c}$) does not follow the Curie—Weiss law very well (see the SI, Figure S11). There are many possible reasons to deviate from the Curie—Weiss behavior at low field, including magnetic impurities, magnetic background, or remanent fields. All of these become negligible at higher fields. Since we primarily want to compare with the effective moment of Eu²⁺ ions, we used 5 T. With larger

applied field, the magnetic phase transition as indicated by the broad transition below 25 K shifts to higher temperatures. From Figure 10b, the compound shows signs of magnetic ordering up to 25 K. The compound does not reach saturation up to a field of 7 T at 2 K where a maximum value of 4.87 $\mu_{\rm B}/{\rm Eu}$ is obtained, suggesting an antiferromagnetic (AFM) ordering with a ferromagnetic component at low temperature.

Electrical Resistivity. The electrical resistivity as a function of temperature and field is shown in Figure 11. The compound exhibits metallic behavior (increasing resistivity with temperature) with a resistivity value (\sim 2 m Ω ·cm) at room temperature. A residual resistance ratio (RRR = R(300 K)/R(2 K)) of 1.142 is observed that suggests the structure is highly disordered and is consistent with the presented structural model. The resistance is not strongly affected by field up to 0.5 T where a small magnetoresistance response is observed near the phase transition. There is a clear phase transition at low T that is concurrent with the magnetic phase transition shown in Figure 10. With higher field, the transition can be seen to shift to higher temperatures (Figure 11b). The increase in resistivity below 50 K could arise from a Kondo effect, but the 4f electrons of Eu are far below the Fermi level. Another possibility is that it might originate from the electron-electron interactions proportional to the degree of disorder.³⁷ The observed small RRR value indicates a relatively small free mean path which is consistent with such a scenario. The Fermi wavevector k_F can be estimated from the carrier density in the free electron model as $k_F^3 = 3\pi^2 n$, which gives $k_F \sim 1.9 \times 10^9 \text{ m}^{-1}$, corresponding to a Fermi wavelength of $\lambda_F = 32$ Å. This can be compared with the mean free path. If each Al cluster is a scattering center, the mean free

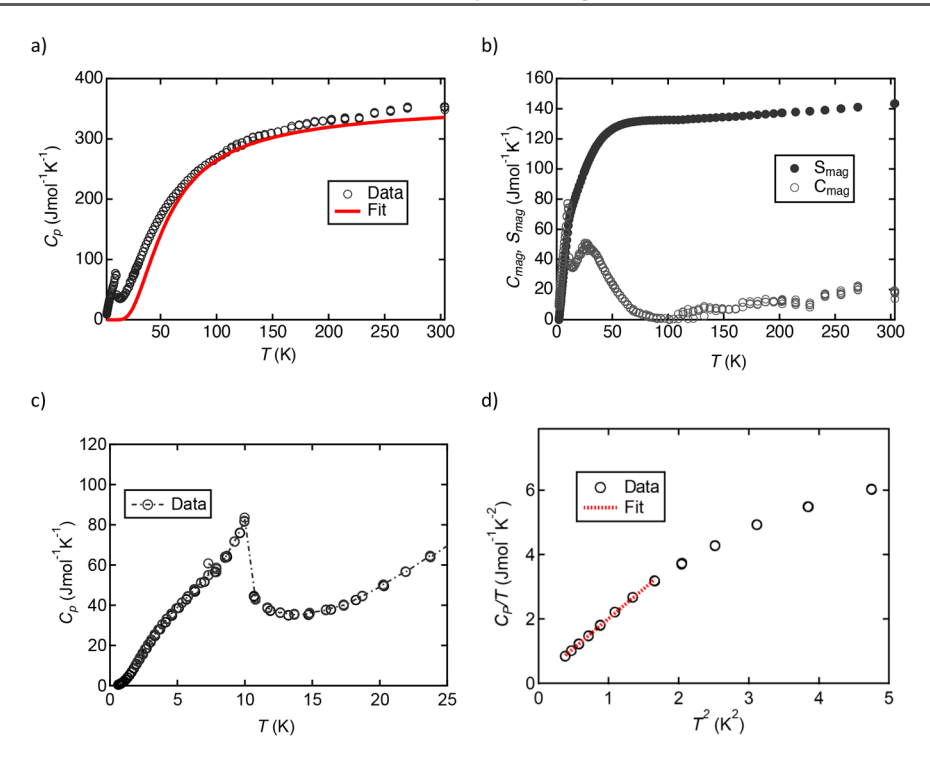


Figure 12. (a) Temperature dependence of the heat capacity $C_p(T)$ of Eu₅Al₃Sb₆ and the Einstein model fit in red ($\theta_E = 181 \text{ K}$). (b) Temperature dependence of the magnetic heat capacity (C_{mag}) and magnetic entropy (S_{mag}). (c) Temperature dependent heat capacity $C_p(T)$ at low temperature. (d) C_p/T vs T^2 with a linear fit yielding $\gamma = 0.17(2)$ J mol⁻¹ K⁻².

path is $l \sim 10$ Å. The ratio of $\frac{\lambda_F}{l} > 1$ supports the possibility of partial charge carrier localization due to disorder.³⁷ Room temperature Hall measurements show that the carriers are electrons with a carrier density of 2.5×10^{20} cm⁻³.

Heat Capacity. The temperature dependence of the heat capacity is shown in Figure 12. The $C_p(T)$ value at room temperature of approximately 354.36 J mol⁻¹ K⁻¹ is close to the predicted high-T Dulong-Petit limit $C_V = 3nR = 351.18$ J mol⁻¹ K⁻¹, where n = 14.08 is the number of atoms per formula unit and R is the gas constant. The $C_p(T)$ data were fit (Figure 12a) using an Einstein model according to the following equation:

Einstein model for heat capacity fitting

$$C_{\text{Einstein}} = 3R \left(\frac{\theta_{\text{E}}}{T}\right)^2 \frac{e^{\theta_{\text{E}}/T}}{\left(e^{\theta_{\text{E}}/T} - 1\right)^2} \tag{1}$$

where R is the gas constant and $\theta_{\rm E}$ is the Einstein temperature (fit yields 181 K). The magnetic heat capacity ($C_{\rm mag}$) is estimated by subtracting the fit from the total heat capacity (Figure 12b) and subsequently integrated to yield $S_{\rm mag}$ according to the equation:

Magnetic entropy calculated from the magnetic heat capacity

$$S_{\text{mag}} = \int_0^T \frac{C_{\text{mag}}}{T} \, dT \tag{2}$$

The measurements show a well-defined peak at 10 K attributed to the magnetic phase transition and a much broader peak around 45 K that arises from the shortcomings of the Einstein model in describing the phonon contribution to the heat capacity. This leads to a greater than expected magnetic entropy. The heat capacity was fit with alternative models (i.e., Debye model, weighted Debye, and Einstein); however, all

models yielded similar fits. To restrict the number of free parameters and keep the model physically sound, the Einstein model fit is chosen because most of the phonon branches are optical in nature for this compound. These models are, in general, huge approximations that assume simplistic phonon dispersion relations and do not always model the heat capacity properly. Proper subtraction of the lattice heat capacity requires detailed DFT phonon calculations or a nonmagnetic analogue of the compound that can be measured and subtracted. We considered the published heat capacity for LaSb³⁸ as an analogue to subtraction of the phonon contributions to the heat capacity; however, the heat capacity exceeds that of Eu_{5.08}Al₃Sb₆ (see SI, Figure S12). The high temperature theoretical limit is given by $S_{\text{mag}} = 5.08 \times R \ln(2S + 1) = 87.8 \text{ J mol}^{-1} \text{ K}^{-1}$, which is much smaller than the observed value of magnetic entropy at room temperature $(143.44 \text{ J mol}^{-1} \text{ K}^{-1})$.

Heat capacity at low temperature from 0.6 to 20 K (Figure 12c) was fit with following equation:

Temperature dependence of heat capacity at low temperature

$$C_{p}(T) = \gamma T + \beta T^{3} \tag{3}$$

The fitting yields $\gamma=0.17(2)~\mathrm{J~mol^{-1}~K^{-2}}$ and $\beta=1.85(1)~\mathrm{J~mol^{-1}~K^{-4}}$. The Sommerfeld coefficient γ per mol of Eu is 34 (4) mJ mol⁻¹ K⁻², which is moderately higher than those of some stable-valent Eu compounds (EuCo₂Si₂³⁹ with 9.6 mJ mol⁻¹ K⁻² and EuRh₂Si₂⁴⁰ with 25 mJ mol⁻¹ K⁻²) and comparable to those of Eu compound with valence fluctuations (EuIr₂Si₂⁴¹ with 33 mJ mol⁻¹ K⁻²). Lower temperature data are needed to obtain a more precise value of γ . While the high Sommerfeld coefficient suggests heavy Fermion behavior of this compound, the defects can also result in an enhancement of the γ term. ⁴²

CONCLUSION

In conclusion, Eu₅Al₃Sb₆ has been successfully synthesized through Sn flux. The crystal structure has been characterized by X-ray diffraction and HRTEM revealing disordered [Al₄] tetrahedral clusters located in an octahedron of Sb atoms. Electronic structure calculations on hypothetical Eu₅Al₄Sb₆ shows the potential for topological behavior in this compound and provides ab initio reasoning for the presence of the disordered Al clusters due to the strong antibonding Al-Sb character near the Fermi level. Mössbauer spectroscopic measurements confirm the ¹⁵¹Eu and ¹²¹Sb local environments and oxidation states. Magnetoresistance measurements show weak dependence with field and reveal semimetallic behavior up to room temperature. Magnetic susceptibility measurements show good agreement with a Curie-Weiss model to yield an effective moment of 7.80 μ_B/mol Eu and suggest antiferromagnetic ordering with a ferromagnetic component. The transition observed in resistivity and heat capacity around 10 K shifts to higher temperatures with applied magnetic field. In magnetization measurements, with large, applied field, the magnetic transition is indicated by a broad increase upon cooling below 25 K. Studies on chemical analogues of this structure type are underway to provide further insight into the structure-property relationship.

ASSOCIATED CONTENT

Supporting Information

The Supporting Information is available free of charge at https://pubs.acs.org/doi/10.1021/acs.chemmater.2c00304.

Additional X-ray diffraction data collection and structural refinement tables, image of the resistivity setup, close up structural views of various coordination sites, and EDS spectrum of a single crystal, inverse susceptibility as a function of field and temperature, and heat capacity compared with LaSb (PDF)

Crystallographic information file for the $Eu_5Al_3Sb_6$ single crystal (CIF)

AUTHOR INFORMATION

Corresponding Author

Susan M. Kauzlarich — Department of Chemistry, University of California, Davis, California 95616, United States;
orcid.org/0000-0002-3627-237X; Email: smkauzlarich@ucdavis.edu

Authors

Allan He – Department of Chemistry, University of California, Davis, California 95616, United States

Zihao Shen – Department of Physics and Astronomy, University of California, Davis, California 95616, United States

Haozhe Wang — Department of Chemistry and Chemical Biology, Rutgers University, Piscataway, New Jersey 08854, United States; © orcid.org/0000-0003-4820-833X

Weiwei Xie — Department of Chemistry and Chemical Biology, Rutgers University, Piscataway, New Jersey 08854, United States

Zhen Wang — Condensed Matter Physics and Materials Science Department, Brookhaven National Laboratory, Upton, New York 11973, United States

Luis Garay – Department of Chemistry, University of California, Davis, California 95616, United States James C. Fettinger — Department of Chemistry, University of California, Davis, California 95616, United States;
orcid.org/0000-0002-6428-4909

Raphaël P. Hermann – Materials Science and Technology Division, Oak Ridge National Laboratory, Oak Ridge, Tennessee 37831, United States; orcid.org/0000-0002-6138-5624

Yimei Zhu — Condensed Matter Physics and Materials Science Department, Brookhaven National Laboratory, Upton, New York 11973, United States; orcid.org/0000-0002-1638-7217

Valentin Taufour – Department of Physics and Astronomy, University of California, Davis, California 95616, United States

Complete contact information is available at: https://pubs.acs.org/10.1021/acs.chemmater.2c00304

Notes

The authors declare no competing financial interest.

ACKNOWLEDGMENTS

This work was supported by NSF DMR-2001156. Z.S. and V.T. acknowledge support from the UC Laboratory Fees Research Program (LFR-20-653926) and the Physics Liquid Helium Laboratory Fund. W.X. and H.Z.W. at Rutgers were supported by NSF- DMR-2053287. The electron microscopy work at BNL was supported by U.S. DOE-BES, Materials Sciences and Engineering Division, under Contract No. DESC0012704. Mössbauer spectral work by R.P.H. was supported by the U.S. Department of Energy (DOE), Office of Science, Office of Basic Energy Sciences (BES), Materials Sciences and Engineering Division. We thank P. Klavins (UCD Physics) for useful discussions.

REFERENCES

- (1) Brown, S. R.; Kauzlarich, S. M.; Gascoin, F.; Snyder, G. J. Yb₁₄MnSb₁₁: New High Efficiency Thermoelectric Material for Power Generation. *Chem. Mater.* **2006**, *18* (7), 1873–1877.
- (2) He, A.; Bux, S. K.; Hu, Y.; Uhl, D.; Li, L.; Donadio, D.; Kauzlarich, S. M. Structural Complexity and High Thermoelectric Performance of the Zintl Phase: Yb₂₁Mn₄Sb₁₈. *Chem. Mater.* **2019**, *31* (19), 8076–8086
- (3) He, A.; Cerretti, G.; Kauzlarich, S. M. The Impact of Site Selectivity and Disorder on the Thermoelectric Properties of $Yb_{21}Mn_4Sb_{18}$ solid Solutions: $Yb_{21}Mn_{4-x}Cd_xSb_{18}$ and $Yb_{21-y}Ca_yMn_4Sb_{18}$. *Mater. Adv.* **2021**, *2* (17), 5764–5776.
- (4) Heremans, J. P.; Jovovic, V.; Toberer, E. S.; Saramat, A.; Kurosaki, K.; Charoenphakdee, A.; Yamanaka, S.; Snyder, G. J. Enhancement of Thermoelectric Efficiency in PbTe by Distortion of the Electronic Density of States. *Science* **2008**, *321* (5888), 554–557.
- (5) He, A.; Wille, E. L. K.; Moreau, L. M.; Thomas, S. M.; Lawrence, J. M.; Bauer, E. D.; Booth, C. H.; Kauzlarich, S. M. Intermediate Yb Valence in the Zintl Phases Yb₁₄MSb₁₁ (M = Zn,Mn,Mg): XANES, Magnetism, and Heat Capacity. *Phys. Rev. Mater.* **2020**, *4*, 114407.
- (6) Sales, B. C.; Khalifaĥ, P.; Enck, T. P.; Nagler, E. J.; Sykora, R. E.; Jin, R.; Mandrus, D. Kondo Lattice Behavior in the Ordered Dilute Magnetic Semiconductor Yb_{14-x}La_xMnSb₁₁. *Phys. Rev. B Condens. Matter Mater. Phys.* **2005**, 72 (20), 1–5.
- (7) Mathieu, J. L.; Latturner, S. E. Zintl Phase as Dopant Source in the Flux Synthesis of $Ba_{1-x}K_xFe_2As_2$ Type Superconductors. *Chem. Commun.* **2009**, 33, 4965–4967.
- (8) Zhu, Z.; Li, M.; Li, J. Topological Semimetal to Insulator Quantum Phase Transition in the Zintl Compounds B A_2X (X = Si,Ge). *Phys. Rev. B* **2016**, *94* (15), 4–7.

- (9) Wendorff, M.; Röhr, C. $Sr_{14}[Al_4]_2[Ge]_3$: Eine Zintl-Phase Mit Isolierten $[Ge]^{4-}$ Und $[Al_4]^{8-}$ Anionen. Z. Naturforsch. **2007**, 62b, 1227–1234.
- (10) Hillebrecht, H.; Ade, M. B₄ Tetrahedra for Aluminum Atoms A Surprising Substitution in T-Borides Ni₂₀Al₃B₆ and Ni₂₀AlB₁₄. *Angew. Chem.* **1998**, 37, 935–938.
- (11) Bergeron, D. E.; Roach, P. J.; Castleman, A. W.; Jones, N. O.; Khanna, S. N. Al Cluster Superatoms as Halogens in Polyhalides and as Alkaline Earths in Iodide Salts. *Science* (80-.) **2005**, 307 (5707), 231–235.
- (12) Castleman, A. W.; Khanna, S. N. Clusters, Superatoms, and Building Blocks of New Materials. *J. Phys. Chem. C* **2009**, *113* (7), 2664–2675.
- (13) Castleman, A. W. From Elements to Clusters: The Periodic Table Revisited. *J. Phys. Chem. Lett.* **2011**, 2 (9), 1062–1069.
- (14) Uhl, W. Tetrahedral Homonuclear Organoelement Clusters and Subhalides of Aluminium, Gallium and Indium. *Naturwissenschaften* **2004**, *91* (7), 305–319.
- (15) Dohmeier, C.; Robl, C.; Tacke, M.; Schnöckel, H. The Tetrameric Aluminum(I) Compound $[\{Al(H_5-C_5Me_5)\}_4]$. Angew. Chem., Int. Ed 1991, 30 (5), 564–565.
- (16) Ovchinnikov, A.; Smetana, V.; Mudring, A. V. Metallic Alloys at the Edge of Complexity: Structural Aspects, Chemical Bonding and Physical Properties *J. Phys.: Condens. Matter* 2020, 32, DOI: 10.1088/1361-648X/ab6b87.
- (17) Zevalkink, A.; Zeier, W. G.; Cheng, E.; Snyder, J.; Fleurial, J. P.; Bux, S. Nonstoichiometry in the Zintl Phase $Yb_{1-\Delta}Zn_2Sb_2$ as a Route to Thermoelectric Optimization. *Chem. Mater.* **2014**, *26* (19), 5710–5717.
- (18) Ertekin, E.; Srinivasan, V.; Ravichandran, J.; Rossen, P. B.; Siemons, W.; Majumdar, A.; Ramesh, R.; Grossman, J. C. Interplay between Intrinsic Defects, Doping, and Free Carrier Concentration in SrTiO₃ Thin Films. *Phys. Rev. B Condens. Matter Mater. Phys.* **2012**, 85 (19), 1–9.
- (19) May, A. F.; Toberer, E. S.; Saramat, A.; Snyder, G. J. Characterization and Analysis of Thermoelectric Transport in n-Type Ba₈Ga_{16-x}Ge_{30+x}. *Phys. Rev. B Condens. Matter Mater. Phys.* **2009**, 80 (12), 1–12.
- (20) Canfield, P. C.; Kong, T.; Kaluarachchi, U. S.; Jo, N. H. Use of Frit-Disc Crucibles for Routine and Exploratory Solution Growth of Single Crystalline Samples. *Philos. Mag.* **2016**, *96* (1), 84–92.
- (21) Shang, R.; Nguyen, A. T.; He, A.; Kauzlarich, S. M. Crystal Structure Characterization and Electronic Structure of a Rare-Earth-Containing Zintl Phase in the Yb-Al-Sb Family: Yb₃AlSb₃. *Acta Crystallogr. Sect. C Struct. Chem.* **2021**, 77, 281–285.
- (22) Dronskowski, R. Computational Chemistry of Solid State Materials: A Guide for Materials Scientists, Chemists, Physicists and Others; Wiley-VCH: 2008.
- (23) Jepsen, O.; Andersen, O. K. *The STUTTGART TB-LMTO Program*; Max Planck-Institut für Festkörperforschung: Stuttgart, Germany, 2000.
- (24) Marshall, M.; Pletikosić, I.; Yahyavi, M.; Tien, H. J.; Chang, T. R.; Cao, H.; Xie, W. Magnetic and Electronic Structures of Antiferromagnetic Topological Material Candidate EuMg₂Bi₂. *J. Appl. Phys.* **2021**, *129* (3), 035106.
- (25) Stegemann, F.; Block, T.; Klenner, S.; Zhang, Y.; Fokwa, B. P. T.; Doerenkamp, C.; Eckert, H.; Janka, O. Structural, Physical, Theoretical and Spectroscopic Investigations of Mixed-Valent Eu₂Ni₈Si₃ and Its Structural Anti-Type Sr₂Pt₃Al₈. *Eur. J. Inorg. Chem.* **2021**, 2021 (37), 3832–3845.
- (26) Giesecke, G.; Pfister, H. Präzisionsbestimmung Der Gitterkonstanten von A III B V -Verbindungen. *Acta Crystallogr.* **1958**, *11* (5), 369–371.
- (27) Radzieowski, M.; Bönnighausen, J.; Janka, O. Synthesis and Magnetic Properties of the Extended RE₄Pd₉Al₂₄ Series (RE = Sc, Y, Ce-Nd, Sm, Gd-Lu). *Zeitschrift für Naturforsch. B* **2020**, 75, 633–641.
- (28) Taylor, J. B.; Calvert, L. D.; Wang, Y. Powder Data for Some New Europium Antimonides and Bismuthides. *J. Appl. Crystallogr.* **1979**, *12* (2), 249–251.

- (29) Brixner, L. H. Structure and Electrical Properties of Some New Rare Earth Arsenides, Antimonides and Tellurides. *J. Inorg. Nucl. Chem.* **1960**, *15* (1–2), 199–201.
- (30) Kawamura, H.; Kumar, V.; Sun, Q.; Kawazoe, Y. Magic Behavior and Bonding Nature in Hydrogenated Aluminum Clusters. *Phys. Rev. B Condens. Matter Mater. Phys.* **2001**, 65 (4), 045406.
- (31) Ichikawa, K.; Ikeda, Y.; Wagatsuma, A.; Watanabe, K.; Szarek, P.; Tachibana, A. Theoretical Study of Hydrogenated Tetrahedral Aluminum Clusters. *Int. J. Quantum Chem.* **2011**, *111* (14), 3548–3555
- (32) Bacalis, N. C.; Metropoulos, A.; Gross, A. Theoretical Study of the O₂ Interaction with a Tetrahedral Al₄ Cluster. *J. Phys. Chem. A* **2010**, 114 (43), 11746–11750.
- (33) Radzieowski, M.; Block, T.; Fickenscher, T.; Zhang, Y.; Fokwa, B. P. T.; Janka, O. Synthesis, Crystal and Electronic Structures, Physical Properties and ¹²¹Sb and ¹⁵¹Eu Mössbauer Spectroscopy of the Alumo-Antimonide Zintl-Phase Eu₅Al₂Sb₆. *Mater. Chem. Front* **2017**, *1* (8), 1563–1572.
- (34) Radzieowski, M.; Block, T.; Klenner, S.; Zhang, Y.; Fokwa, B. P. T.; Janka, O. Synthesis, Crystal and Electronic Structure, Physical Properties and ¹²¹Sb and ¹⁵¹Eu Mössbauer Spectroscopy of the Eu₁₄AlPn₁₁ Series (Pn = As, Sb). *Inorg. Chem. Front* **2019**, 6 (1), 137–147.
- (35) Manchon, A.; Koo, H. C.; Nitta, J.; Frolov, S. M.; Duine, R. A. New Perspectives for Rashba Spin-Orbit Coupling. *Nat. Mater.* **2015**, *14* (9), 871–882.
- (36) Pruitt, R. A.; Marshall, S. W.; O'Donnell, C. M. Mössbauer Spectroscopy in Group-III Antimonides. *Phys. Rev. B* **1970**, 2 (7), 2383–2390.
- (37) Herranz, G.; Martínez, B.; Fontcuberta, J.; Sánchez, F.; Ferrater, C.; García-Cuenca, M. V.; Varela, M. Enhanced Electron-Electron Correlations in Nanometric SrRuO₃ Epitaxial Films. *Phys. Rev. B Condens. Matter Mater. Phys.* **2003**, *67* (17), 1–8.
- (38) Wallace, W. E.; Deenadas, C.; Thompson, A. W.; Craig, R. S. Low Temperature Heat Capacities of PrBi, PrSb, LaBi and LaSb, Crystal Field Effects in PrBi and PrSb. *J. Phys. Chem. Solids* **1971**, 32 (4), 805–813
- (39) Seiro, S.; Kummer, K.; Vyalikh, D.; Caroca-Canales, N.; Geibel, C. Anomalous Susceptibility in Single Crystals of EuCo₂Si₂ with Trivalent Eu: Influence of Excited J Multiplets. *Phys. Status Solidi Basic Res.* **2013**, 250 (3), 621–625.
- (40) Seiro, S.; Geibel, C. From Stable Divalent to Valence-Fluctuating Behaviour in $Eu(Rh_{1-x}Ir_x)_2Si_2$ Single Crystals. *J. Phys.: Condens. Matter* **2011**, 23 (37), 375601.
- (41) Seiro, S.; Prots, Y.; Kummer, K.; Rosner, H.; Cardoso Gil, R.; Geibel, C. Charge, Lattice and Magnetism across the Valence Crossover in EuIr₂Si₂ Single Crystals. *J. Phys.: Condens. Matter* **2019**, *31* (30), 305602.
- (42) Bevk, J. The Effect of Lattice Defects on the Low-Temperature Heat Capacity of Copper. *Philos. Mag.* **1973**, 28 (6), 1379–1390.